

# Physics-Constrained Inverse Acoustic Reconstruction via Projections Onto Convex Sets (POCS)

Chanho Park<sup>a</sup>, Yeachan Kwak<sup>a</sup>, Seongim Choi<sup>a,\*</sup>

<sup>a</sup>Gwangju Institute of Science and Technology, Department of Mechanical Engineering, Gwangju 61005, South Korea

## Abstract

The reconstruction of coherent acoustic fields from sparse, irregular, or occluded sensor measurements remains a critical challenge in experimental aeroacoustics. Conventional geometric interpolation techniques, such as Kriging and Inverse Distance Weighting (IDW), rely on smoothness priors that minimize local curvature. While statistically robust for diffusive fields, these methods inherently suppress oscillatory wave physics, failing to capture essential features such as diffraction patterns and interference fringes within data gaps. To overcome these limitations, this paper proposes a physics-constrained inverse solver based on the method of Projections Onto Convex Sets (POCS). We reformulate the reconstruction problem as finding the intersection between the set of observation-consistent fields and the manifold of solutions satisfying the acoustic dispersion relation. The proposed iterative algorithm utilizes a “Resonant Tapered Filter” in the spectral domain to regenerate missing spectral content, operating entirely without training data or precomputed basis functions. A systematic benchmarking across five canonical scenarios—including cylinder scattering, Doppler-shifted sources, and rotating quadrupoles—demonstrates that the method significantly outperforms standard interpolants in structural fidelity. The solver achieves superior Structural Similarity Index (SSIM) scores, successfully recovering complex topological features like spiral arms and directional lobes that are lost by geometric methods. This framework serves as a robust tool for the physically plausible presumption of acoustic fields in the presence of large shadow zones.

## Keywords:

Acoustic reconstruction, Inverse problems, POCS, Aeroacoustics, Sparse sensing

## 1. Introduction

Recovering coherent acoustic information from sparse or incomplete measurements is a central challenge in experimental acoustics and aeroacoustics. This problem spans applications ranging from wind-tunnel testing and machinery noise diagnostics to urban sound mapping and environmental monitoring [1–5]. In many scenarios, practical constraints inevitably create “shadow zones” where microphones cannot be placed: bulky models in wind tunnels, structural supports, rotating machinery, or safety limitations lead to large, contiguous gaps in the measurement aperture [3, 6]. Even with high sensor counts, the combination of sparse arrays and acoustic shielding often leaves critical regions unobserved. Yet, it is precisely in these gaps that important physics occur creeping-wave diffraction behind obstacles, interference patterns in wakes, or destructive interference nodes [6, 7]. Without estimation, these phenomena remain invisible, rendering subsequent modal analysis or source characterization incomplete [5, 8]. This necessitates methods capable of estimating the field in such gaps to provide a physically consistent context for the available data.

Current approaches to this problem generally fall into three categories, each with distinct limitations regarding large data gaps.

The first strategy treats acoustic pressure as a generic scalar field, applying geometric interpolation schemes such as inverse-distance weighting (IDW) [9], radial basis functions (RBF) [10, 11], or Kriging [4]. While robust for urban noise mapping [12, 13], these methods implicitly assume the field varies “smoothly” by minimizing curvature or Laplacian energy. Effectively, they solve a Laplace-like problem in the gap. However, real acoustic fields satisfy the Helmholtz equation, where the Laplacian is proportional to the pressure itself. Consequently, geometric interpolation produces overly smooth, diffusive estimations that erase oscillatory wave phenomena like interference fringes. Empirical studies confirm that such methods fail to reproduce fine acoustic details without extremely high sensor densities [4].

The second strategy exploits the physics of wave propagation directly. Techniques such as Nearfield Acoustic Holography (NAH) [6, 7], Statistically Optimized NAH (SONAH) [14], and the Helmholtz Equation Least Squares (HELS) method [15, 16] reconstruct fields by encoding the wave equation and Green’s functions. While these methods theoretically offer high fidelity, the underlying inverse problems are typically ill-conditioned [17]. They generally require well-posed boundary configurations; large “holes” in the aperture or strong occlusions can cause severe noise amplification and degradation of the solution [5]. Similarly, beamforming and modal decomposition methods (e.g., POD/SPOD) rely on the presence of structures within the

\*Corresponding author: Seongim Choi, Email: schoi1@gist.ac.kr

measured data or stationarity assumptions that are violated in the presence of scatterers [18, 19].

The third, emerging strategy involves machine learning. Convolutional Neural Networks (CNNs) and Physics-Informed Neural Networks (PINNs) have shown promise in mapping measured fields to target fields [20–22]. Generative models can extend effective bandwidths and reconstruct impulse responses [23, 24]. However, these approaches are data-hungry and prone to poor generalization outside their training distribution [25]. Assembling large, diverse training sets for bespoke experimental configurations remains a significant bottleneck.

To bridge the gap between analytical rigor and data flexibility, we introduce a lightweight estimation framework based on Projections Onto Convex Sets (POCS). POCS is an iterative method for enforcing multiple constraints simultaneously [26, 27]. A classic example is the Papoulis–Gerchberg algorithm for band-limited signal extrapolation [28]. We generalize this philosophy to the acoustic domain by defining two constraint sets:

1. **A Data Consistency** set: Fields that match measured values at sensor locations.
2. **A Physics Consistency** set: Fields whose spatial Fourier spectra lie on the **Acoustic Dispersion Manifold** (or Dispersion Surface).

Our algorithm iterates between these projections: enforcing measurements in the physical domain and applying a “Resonant Tapered Filter” in the wavenumber domain that isolates the physics-compliant dispersion surface. Unlike ML approaches, this procedure requires no training data; the only model is the acoustic wave equation itself. At convergence, the method yields a field that respects the measurements and is spectrally concentrated on the Helmholtz manifold.

It is important to clarify the scope of this method. Rather than replacing high-fidelity metrology or full-wave simulations in highly complex scattering environments [5], this approach complements existing techniques by offering a physically consistent means of estimating coherent acoustic fields within measurement gaps. With minimal computational cost, it provides wave-based continuity in regions where traditional geometric interpolation typically produces overly smoothed results.

The contributions of this paper are threefold. First, we formulate a training-free POCS algorithm that combines sparse data enforcement with a soft spectral dispersion constraint. Second, we systematically benchmark the method against standard interpolants across five canonical scenarios: cylinder scattering, dipole shielding, Doppler-shifted sources, rotating quadrupoles, and full-field reconstruction from sparse microphone arrays. Third, we analyze the solver’s behavior, demonstrating that embedding a minimal wave-physics prior enables the recovery of diffractive and interference structures that are completely missed by traditional methods.

## 2. Methodology

### 2.1. Problem Formulation: The Inverse Acoustic Reconstruction

The recovery of coherent acoustic fields from spatially sparse observations represents a critical inverse problem in aeroacoustics. Whether due to physical shielding, limited sensor inventory, or computational domain truncation, experimental datasets often contain large, contiguous regions of missing data (shadow zones). Standard reconstruction techniques, such as Delay-and-Sum Beamforming or Spectral Proper Orthogonal Decomposition (SPOD), operate under the assumption of statistical stationarity or free-field radiation conditions that are violated in the presence of scatterers and occlusions [18, 29]. Crucially, these methods lack an explicit mechanism to *generate* physical wave information in regions where no measurements exist.

We reformulate this challenge not as a signal interpolation task, but as an “ill-posed inverse source problem”. We seek a unique field solution that simultaneously satisfies the sparse boundary data and the governing partial differential equation (the wave equation). This requires finding the intersection of two distinct manifolds in the solution space: the affine subspace of observation-consistent fields and the spectral manifold of physically admissible dispersion.

#### 2.1.1. Measurement Model and Sparsity

Let  $\mathbf{q} \in \mathbb{C}^N$  represent the discretized complex pressure field vectorized over a spatio-temporal lattice  $\Omega \times T$ . The acquisition process is modeled as a linear degradation operator:

$$\mathbf{y} = \mathcal{M}\mathbf{q} + \mathbf{n}, \quad (1)$$

where:

- $\mathbf{y} \in \mathbb{C}^N$  is the measurement vector, populated only at sensor locations and zero-padded elsewhere.
- $\mathcal{M} \in \{0, 1\}^{N \times N}$  is the Sampling Projection Operator. It is a diagonal binary matrix where  $\mathcal{M}_{ii} = 1$  if index  $i$  corresponds to a sensor location  $\mathbf{x} \in \Omega_{\text{sensor}}$ , and  $\mathcal{M}_{ii} = 0$  if  $\mathbf{x} \in \Omega_{\text{gap}}$ . Note that  $\mathcal{M}$  is idempotent ( $\mathcal{M}^2 = \mathcal{M}$ ).
- $\mathbf{n} \sim \mathcal{CN}(0, \sigma_n^2 \mathbf{I})$  denotes complex circular Gaussian noise.

#### 2.1.2. The Ill-Posedness and Null Space

The inverse problem of recovering  $\mathbf{q}$  from  $\mathbf{y}$  is ill-posed due to the non-trivial null space  $\mathcal{N}(\mathcal{M})$ . Any field component  $\mathbf{q}_\perp$  residing entirely within the shadow zone satisfies  $\mathcal{M}\mathbf{q}_\perp = \mathbf{0}$ , leading to infinite admissible solutions of the form  $\hat{\mathbf{q}} = \mathbf{q}_{\text{true}} + \alpha\mathbf{q}_\perp$ .

Classic interpolation methods (Linear, Kriging, Radial Basis Functions) regularize this singularity by imposing a minimum-curvature constraint [30, 31]. Implicitly or explicitly, they solve:

$$\min_{\mathbf{q}} \|\nabla^2 \mathbf{q}\|_2^2 \quad \text{s.t.} \quad \mathcal{M}\mathbf{q} = \mathbf{y}. \quad (2)$$

This regularization promotes solutions that satisfy the Laplace equation,  $\nabla^2 \mathbf{q} \approx 0$ , which governs diffusive transport (e.g., heat transfer). However, this is fundamentally inconsistent with wave physics. Acoustic fields are oscillatory solutions to the Helmholtz equation ( $\nabla^2 \mathbf{q} + k^2 \mathbf{q} = 0$ ), implying that the local curvature is proportional to the field amplitude ( $|\nabla^2 \mathbf{q}| \propto k^2 |\mathbf{q}|$ ). By minimizing curvature, standard interpolation forces the reconstructed wave amplitude to decay exponentially within the gap, effectively erasing the diffractive interference patterns required to fill the shadow zone.

### 2.1.3. Physics-Constrained Variational Formulation

To select the physically admissible solution from the infinite set of mathematically valid interpolants, we introduce a regularization term based on the ‘‘Acoustic Dispersion Manifold’’. In the frequency-wavenumber domain, a free-propagating acoustic wave must reside on the surface of a cone defined by the dispersion relation  $\|\mathbf{k}\|_2 = \omega/c_0$ .

We define the reconstruction as the solution to the following variational optimization problem:

$$\mathbf{q}^* = \underset{\mathbf{q}}{\operatorname{argmin}} \left( \underbrace{\|\mathcal{M}\mathbf{q} - \mathbf{y}\|_2^2}_{\mathcal{J}_{\text{data}}: \text{Data Fidelity}} + \lambda \underbrace{\mathcal{R}_{\text{phys}}(\mathbf{q})}_{\mathcal{J}_{\text{phys}}: \text{Spectral Prior}} \right). \quad (3)$$

The physics prior  $\mathcal{R}_{\text{phys}}$  penalizes spectral energy that deviates from the theoretical dispersion shell. Let  $\hat{q}(\mathbf{k}, \omega)$  denote the multidimensional Fourier transform of the field. The penalty is quantified as:

$$\mathcal{R}_{\text{phys}}(\mathbf{q}) = \int_{\Omega_\omega} \int_{\Omega_k} |\hat{q}(\mathbf{k}, \omega)|^2 \cdot \mathcal{W}(\mathbf{k}, \omega) d\mathbf{k} d\omega, \quad (4)$$

where the spectral weighting function  $\mathcal{W}$  is derived from a Gaussian potential well centered on the dispersion surface:

$$\mathcal{W}(\mathbf{k}, \omega) = 1 - \exp\left(-\frac{(\|\mathbf{k}\|_2 - \omega/c_0)^2}{2\sigma_k^2}\right). \quad (5)$$

This formulation provides the theoretical basis for the ‘‘Resonant Tapered Filter’’ utilized in our iterative solver. The exponential term acts as a soft characteristic function for the acoustic manifold. Crucially, the bandwidth parameter  $\sigma_k$  is not merely a numerical tuning factor but a physical necessity imposed by the ‘‘Heisenberg Uncertainty Principle’’ ( $\sigma_x \sigma_k \geq 1/2$ ) [32]. To spatially confine the reconstruction to a finite gap of size  $L_{\text{gap}}$ , the spectral support cannot be a delta function (a perfect circle); it must possess a finite thickness  $\sigma_k \propto 1/L_{\text{gap}}$  to allow for the diffraction of energy into the shadow zone.

## 2.2. Physics-Constrained Alternating Projections (The Solver)

The reconstruction problem is geometrically formulated as finding a vector  $\mathbf{q}$  in the Hilbert space  $\mathcal{H} = \mathbb{C}^N$  that lies at the intersection of two fundamental constraint sets:

1.  $C_{\text{data}}$ : The affine subspace of fields consistent with the sensor measurements.

2.  $C_{\text{phys}}$ : The manifold of fields satisfying the acoustic dispersion relation.

Since  $C_{\text{phys}}$  represents a complex spectral dependency rather than a simple convex set, we employ an iterative ‘‘Alternating Projection’’ framework. This approach seeks a fixed point  $\mathbf{q}^*$  that balances data fidelity with physical admissibility.

Let  $\mathcal{P}_{\text{data}}$  and  $\mathcal{P}_{\text{phys}}$  denote the projection operators onto the data and physics sets, respectively. We define the composite operator  $\mathcal{T} = \mathcal{P}_{\text{data}} \circ \mathcal{P}_{\text{phys}}$ . The reconstruction seeks a fixed point  $\mathbf{q} = \mathcal{T}(\mathbf{q})$ . To ensure convergence and accelerate the propagation of information into the shadow zone, we utilize a ‘‘Relaxed Averaged Projection’’ scheme. Let  $\mathbf{q}^{(n)}$  denote the estimated field at iteration  $n$ . The update rule is given by:

$$\mathbf{q}^{(n+1)} = (1 - \beta)\mathbf{q}^{(n)} + \beta\mathcal{T}(\mathbf{q}^{(n)}) \quad (6)$$

Rearranging terms yields the iterative update implemented in our solver:

$$\mathbf{q}^{(n+1)} = \mathbf{q}^{(n)} + \beta [\mathcal{P}_{\text{data}}(\mathcal{P}_{\text{phys}}(\mathbf{q}^{(n)})) - \mathbf{q}^{(n)}]. \quad (7)$$

Here,  $\beta \in [0, 2]$  is the relaxation parameter. We employ an ‘‘over-relaxation strategy’’ ( $\beta \approx 1.8$ ), which emphasizes the innovation term (the difference between the projected and current state), thereby forcing the solution rapidly into the null space  $\Omega_{\text{gap}}$ .

### 2.2.1. Projection 1: Data Consistency ( $\mathcal{P}_{\text{data}}$ )

The data projection is an orthogonal projection onto the affine subspace defined by the measurement operator  $\mathcal{M}$ . It strictly enforces the observed values at sensor locations while acting as the identity operator in the unobserved gap.

$$C_{\text{data}} = \{\mathbf{q} \in \mathcal{H} \mid \mathcal{M}\mathbf{q} = \mathbf{y}\} \quad (8)$$

The projection operator  $\mathcal{P}_{\text{data}}$  acts on an arbitrary input field  $\mathbf{u} \in \mathcal{H}$  as follows:

$$\mathcal{P}_{\text{data}}(\mathbf{u}) = \mathbf{y} + (\mathcal{I} - \mathcal{M})\mathbf{u}, \quad (9)$$

where we assume  $\mathbf{y}$  is zero-padded such that  $\mathbf{y}(\mathbf{x}) = 0$  for all  $\mathbf{x} \notin \Omega_{\text{sensor}}$ . This formulation ensures that at every iteration  $n$ ,  $\mathbf{q}^{(n)}(\mathbf{x}) \equiv \mathbf{y}(\mathbf{x})$  for all valid sensors, preventing the solver from altering ground truth data.

### 2.2.2. Projection 2: Soft Spectral Physics Constraint ( $\mathcal{P}_{\text{phys}}$ )

The physics projection restricts the solution to the Acoustic Manifold. In a strictly convex formulation, this would require the spatio-temporal Fourier coefficients  $\hat{q}(\mathbf{k}, \omega)$  to be non-zero only on the dispersion cone surface  $\|\mathbf{k}\| = \omega/c_0$ . However, imposing a hard ‘‘brick-wall’’ cutoff in the frequency domain induces severe Gibbs oscillations (ringing artifacts) in the spatial domain due to the finite aperture [33].

Instead, we define  $\mathcal{P}_{\text{phys}}$  as a ‘‘Soft Spectral Projection’’ utilizing a ‘‘Resonant Tapered Filter’’. Let  $\mathcal{F}$  denote the multidimensional Discrete Fourier Transform (DFT). The projection acts on an input field  $\mathbf{u}$  as:

$$\mathcal{P}_{phys}(\mathbf{u}) = \mathcal{F}^{-1} \{ \mathbf{H} \odot \mathcal{F}\{\mathbf{u}\} \} \quad (10)$$

where  $\odot$  denotes the Hadamard (element-wise) product [34]. The spectral filter kernel  $\mathbf{H}$  is derived from a Gaussian regularization of the dispersion error:

$$H(\mathbf{k}, \omega) = \exp\left(-\frac{\mathcal{D}(\mathbf{k}, \omega)^2}{2\sigma_k^2}\right), \quad (11)$$

with  $\mathcal{D}(\mathbf{k}, \omega) = \left| \|\mathbf{k}\|_2 - \frac{\omega}{c_0} \right|$ .

Here,  $\mathcal{D}(\mathbf{k}, \omega)$  represents the spectral distance to the physically admissible dispersion surface.

**Connection to Discretization:** The spectral bandwidth parameter  $\sigma_k$  is not arbitrary; it is intrinsically linked to the discrete resolution of the computational lattice. To ensure the filter kernel is resolvable on the frequency grid, we parameterize  $\sigma_k$  as a scalar multiple  $\alpha$  of the fundamental wavenumber bin size  $\Delta k = \frac{2\pi}{L}$ :

$$\sigma_k = \alpha \cdot \Delta k \quad (12)$$

This formulation, utilized in the automated tuning step, ensures that the physics constraint scales invariantly with the domain size  $L$  and grid resolution. The parameter  $\alpha$  (typically  $\alpha \in [0.5, 5.0]$ ) governs the stiffness of the physics prior: low  $\alpha$  enforces strict plane-wave propagation, while high  $\alpha$  admits the broader spectral support required to reconstruct diffractive wavefront curvature within the shadow zone.

### 2.3. Automated Hyperparameter Tuning via Empirical Risk Minimization

A critical challenge in inverse problems is the selection of the regularization parameter  $\alpha$  (which governs the spectral bandwidth  $\sigma_k$ ) and the stopping criterion  $N_{iter}$ . Heuristic tuning is prone to overfitting, where the solver minimizes error on the visible sensors but fails to generalize into the shadow zone. To eliminate subjectivity, we implement a fully automated, data-driven calibration strategy based on “Hold-Out Cross-Validation”.

#### 2.3.1. Optimal Regularization via Surrogate Gap Minimization

We determine the optimal physics compliance  $\alpha^*$  by simulating the reconstruction task on a subset of the known data. Let  $\Omega_{valid}$  denote the set of spatial indices where measurements exist. We partition this domain into two disjoint sets: a training aperture  $\Omega_{train}$  and a validation aperture  $\Omega_{val}$ , such that  $\Omega_{train} \cup \Omega_{val} = \Omega_{valid}$  and  $\Omega_{train} \cap \Omega_{val} = \emptyset$ .

This partition defines two distinct masking operators,  $\mathcal{M}_{train}$  and  $\mathcal{M}_{val}$ , where:

$$(\mathcal{M}_{train})_{ii} = \begin{cases} 1 & \text{if } i \in \Omega_{train} \\ 0 & \text{otherwise} \end{cases} \quad (13)$$

We define a “Training Gap” that mimics the geometry of the true shadow zone. We then solve the inverse problem for a discrete sweep of candidate parameters  $\Lambda = \{\alpha_1, \dots, \alpha_m\}$ . The optimal parameter is selected to minimize the normalized reconstruction error on the held-out validation sensors. This forms the following optimization objective:

$$\begin{aligned} \alpha^* &= \underset{\alpha \in \Lambda}{\operatorname{argmin}} \mathcal{L}(\alpha), \\ \text{where } \mathcal{L}(\alpha) &= \frac{\|\mathcal{M}_{val} (\mathcal{T}_\alpha^N (\mathcal{M}_{train} \mathbf{y}) - \mathbf{y})\|_2}{\|\mathcal{M}_{val} \mathbf{y}\|_2} \end{aligned} \quad (14)$$

Here,  $\mathcal{T}_\alpha^N$  denotes the application of the POCS operator with parameter  $\alpha$  for  $N$  iterations. By minimizing the error on the hidden validation set  $\Omega_{val}$ , we effectively minimize the generalization error, ensuring the chosen bandwidth is robust enough to extrapolate into the true unknown void.

#### 2.3.2. Geometric Scaling Law for Convergence Control

The Alternating Projection operator acts as a pseudo-diffusive transport mechanism; information propagates from the valid boundary  $\partial\Omega_{valid}$  into the null space  $\Omega_{gap}$  at a finite rate determined by the filter bandwidth. Consequently, the required iteration count is not a universal constant but depends on the physical characteristic length of the gap.

We quantify this length scale using the “Chebyshev Radius”  $R_{gap}$ , defined as the  $L_\infty$  distance from the deepest point in the shadow zone to the nearest valid sensor. Mathematically, if  $d(\mathbf{x}, \Omega)$  represents the Euclidean distance from a point  $\mathbf{x}$  to a set  $\Omega$ , the radius is:

$$R_{gap} = \sup_{\mathbf{x} \in \Omega_{gap}} d(\mathbf{x}, \Omega_{valid}) \quad (15)$$

In our implementation, this is computed efficiently via the Euclidean Distance Transform (EDT). We assume that the necessary iterations  $N$  scale linearly with the gap size for a fixed propagation speed. We first determine the optimal iteration count  $N_{train}^*$  for the surrogate training gap (which has a known radius  $R_{train}$ ) during the cross-validation phase. The stopping criterion for the true reconstruction is then derived via linear scaling:

$$N_{real}^* = \left\lceil N_{train}^* \times \frac{R_{real}}{R_{train}} \right\rceil \quad (16)$$

This “Geometric Scaling Law” ensures the solver terminates exactly when the reconstructed wavefronts have had sufficient time to traverse the shadow zone, mitigating the risk of numerical dissipation associated with excessive iteration.

## 3. Evaluation Methodology

### 3.1. Baseline Methodologies for Comparative Analysis

To rigorously assess the performance of the proposed physics-constrained POCS solver, we benchmark it against four

distinct classes of reconstruction techniques. These baselines represent the standard geometric, statistical, and physics-based approaches currently employed in experimental aeroacoustics.

The first class of baselines treats field reconstruction as a multivariate interpolation problem, ignoring the underlying wave equation.

### Linear Barycentric Interpolation

This method constructs a Delaunay tessellation of the valid sensor locations [35]. For any query point  $x$  within the convex hull of a simplex (triangle) formed by sensors  $\{x_1, x_2, x_3\}$ , the field is reconstructed as a convex combination of the nodal values:

$$q(x) = \sum_{i=1}^3 \lambda_i(x) q(x_i), \quad \text{s.t.} \quad \sum \lambda_i = 1, \lambda_i \geq 0 \quad (17)$$

where  $\lambda_i$  are the barycentric coordinates. While robust, this method enforces  $C^0$  continuity and implies zero curvature ( $\nabla^2 q = 0$ ) within the gap elements, which is physically inconsistent with the oscillatory nature of acoustic waves where  $\nabla^2 q \propto -k^2 q$ .

### Inverse Distance Weighting (IDW)

To model diffusive decay, we employ Sheppard's method (IDW) [36], which estimates the field at a gap point  $x$  as a weighted average of the  $K$ -nearest valid sensors. The weights decay according to a power law:

$$q(x) = \frac{\sum_{j=1}^K w_j(x) q(x_j)}{\sum_{j=1}^K w_j(x)}, \quad \text{with} \quad w_j(x) = \frac{1}{\|x - x_j\|_2^p} \quad (18)$$

In our benchmarks, we utilize a power parameter  $p = 2.0$ . While IDW provides smooth gradients, the kernel is strictly isotropic and real-valued, meaning it cannot capture the phase progression or directionality of a propagating wavefront.

### Radial Basis Function (RBF) Kriging

For sparse extrapolation tasks, we employ a global interpolation using Radial Basis Functions (often referred to as Kriging in geostatistics). The field is approximated as a weighted sum of radial kernels  $\phi(r)$  centered at the measurement points:

$$q(x) = \sum_{j=1}^N w_j \phi(\|x - x_j\|_2) \quad (19)$$

We utilize a cubic kernel  $\phi(r) = r^3$  to enforce  $C^2$  smoothness. While effective for fitting smooth potential fields, RBFs inherently suppress high-wavenumber oscillations in data-sparse regions, resulting in the "smooth blur" artifacts observed in the results.

### 3.2. Quantitative Evaluation Metrics

To provide a robust statistical assessment of the reconstruction accuracy, we define three error metrics computed over the masked gap region  $\Omega_{gap}$ :

First, the Normalized  $L_2$  Error measures the global energy difference between the reconstructed field  $q_{rec}$  and the ground truth  $q_{true}$ :

$$E_{L_2} = \frac{\|q_{rec} - q_{true}\|_{\Omega_{gap}}}{\|q_{true}\|_{\Omega_{gap}}} \times 100\% \quad (20)$$

Second, to quantify the local pointwise reconstruction accuracy, we compute the Mean Absolute Error (MAE):

$$MAE = \frac{1}{N_{gap}} \sum_{x \in \Omega_{gap}} |q_{rec}(x) - q_{true}(x)| \quad (21)$$

where  $N_{gap}$  is the total number of grid points within the shadow zone. Unlike the  $L_2$  norm, which disproportionately penalizes large outliers, MAE provides a linear assessment of the average amplitude deviation.

Third, to assess the topological accuracy of the wavefronts (independent of pure amplitude scaling), we utilize the Structural Similarity Index (SSIM) [37]. Unlike  $L_2$  or MAE, which are sensitive to small phase misalignments, SSIM quantifies the perceived structural degradation:

$$SSIM(x, y) = \frac{(2\mu_x\mu_y + c_1)(2\sigma_{xy} + c_2)}{(\mu_x^2 + \mu_y^2 + c_1)(\sigma_x^2 + \sigma_y^2 + c_2)} \quad (22)$$

where  $\mu$  and  $\sigma$  represent the local mean and variance, respectively. Higher SSIM values (closer to 100%) indicate better preservation of the diffractive wave patterns.

## 4. Results and Discussion

### 4.1. Translating Dipole with Acoustic Shielding

The first benchmark evaluates the reconstruction of a non-monopole source with complex directivity. We simulate a dipole source ( $f_0 = 5$  kHz) translating horizontally across the domain. A triangular region at the bottom of the domain is masked, representing an acoustic shield or a breakdown in sensor coverage. This case challenges the solver to reconstruct the destructive interference nodes inherent to dipole radiation, which geometric interpolation methods typically smooth over.

The reconstruction results are visualized in Figure 1. The ground truth (Fig. 1a) displays the characteristic dual-lobe radiation pattern of a vertical dipole, with a distinct node of silence along the horizontal axis.

The interpolation baselines (Fig. 1b-d) fail to capture the dipole physics. Because Linear interpolation, IDW, and Kriging rely on local averaging, they effectively "fill" the nodal line with energy from the surrounding lobes. This results in a non-physical, smeared wavefront that resembles a monopole source rather than a dipole. They destroy the phase cancellation information essential for identifying the source type.

In contrast, the proposed POCS method (Fig. 1e) accurately reconstructs the dipole directivity within the gap. The spectral physics prior enforces the correct dispersion relation, allowing the solver to extend the interference fringes (the "arms" of the dipole field) deep into the shielded region without the diffusive blurring seen in the baselines.

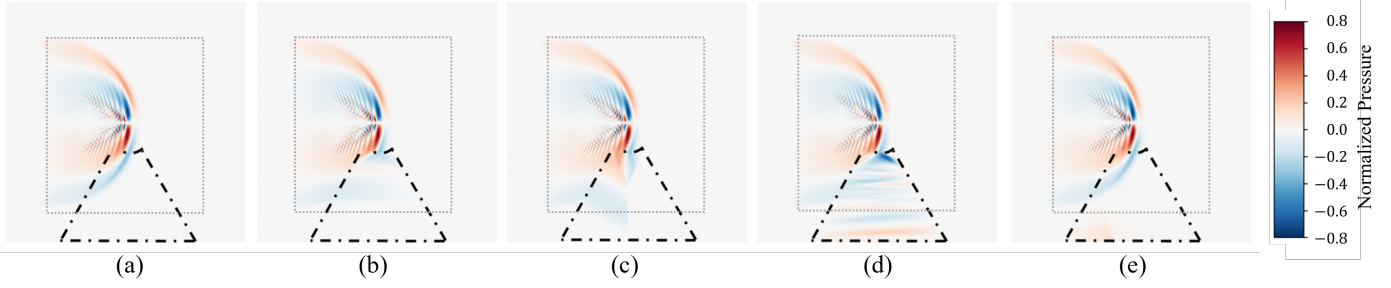


Figure 1: Reconstruction of the translating dipole field (5 kHz) obscured by a triangular gap. The gray border denotes the sponge layer. (a) Ground Truth showing dipole directivity. (b) Linear Interpolation. (c) Inverse Distance Weighting (IDW). (d) Kriging (Cubic RBF). (e) Proposed Physics-Constrained POCS. The proposed method (e) is the only approach that correctly reconstructs the interference fringes inside the gap, whereas baselines (b-d) smear the field into a monopole-like blob.

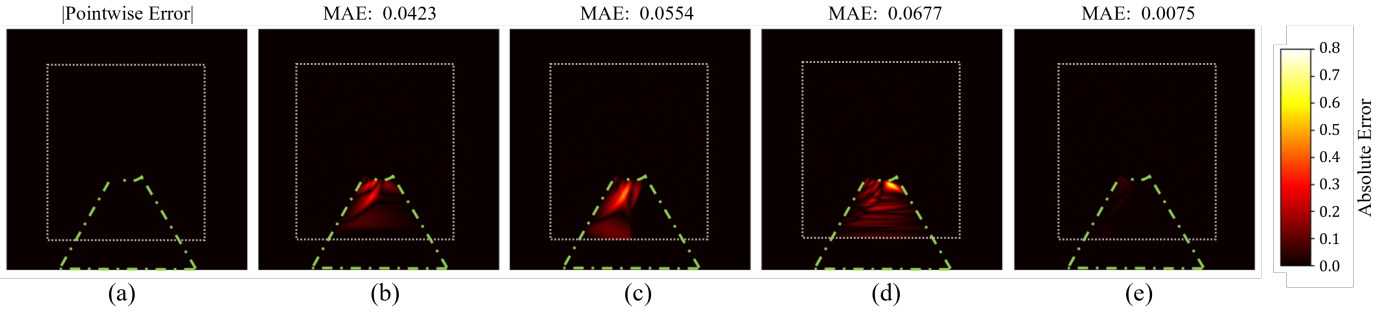


Figure 2: Absolute pointwise error distributions for the dipole benchmark. The gray border denotes the sponge layer. (a) Reference Scale. (b) Linear Interpolation. (c) IDW. (d) Kriging. (e) Proposed Method. The proposed method achieves almost an order-of-magnitude reduction in Mean Absolute Error.

Table 1: Quantitative error metrics for the Translating Dipole benchmark. The proposed method reduces the MAE by a factor of 5-9 compared to standard interpolation.

Method	MAE	$L_2$ Error (%)	SSIM (%)
Linear	0.0423	80.0%	57.0%
IDW	0.0554	122.3%	64.4%
Kriging	0.0677	130.8%	44.1%
Proposed (POCS)	0.0075	14.6%	84.6%

Table 1 compares the statistical performance of the reconstruction methods.

The proposed method achieves a Mean Absolute Error (MAE) of 0.0075, which is approximately 5 to 9 times lower than the geometric baselines (Linear: 0.0423, Kriging: 0.0677). In terms of global fidelity, the proposed method achieves a Normalized L2 Error of 14.6%, compared to 80.0% for Linear interpolation and greater than 100% for IDW and Kriging. Furthermore, the SSIM score is 84.6%, the highest among all methods, confirming that the intricate phase structure of the dipole field is preserved.

#### 4.2. Doppler Effect from a Moving Source

The second benchmark introduces spectral complexity through source motion. We simulate a monopole source translating horizontally at Mach  $M = 0.5$  (171.5 m/s), creating a strong Doppler shift. The wavefronts compress ahead of the source (high frequency) and expand behind it (low frequency). A large angular sector ( $60^\circ$  to  $120^\circ$ ) is masked to simulate a

Table 2: Quantitative error metrics for the Doppler Moving Source benchmark. The proposed method excels in recovering the high-frequency content ahead of the source.

Method	MAE	$L_2$ Error (%)	SSIM (%)
Linear	0.0913	76.9%	59.4%
IDW	0.0897	69.6%	69.1%
Kriging	0.1336	106.9%	52.3%
Proposed (POCS)	0.0437	38.8%	80.2%

limited observation aperture, forcing the solver to reconstruct both the compressed and rarefied waves simultaneously.

Figure 3 presents the results. The ground truth (Fig. 3a) clearly shows the asymmetric wavelength distribution characteristic of the Doppler effect.

The interpolation baselines (Fig. 3b-d) fail to capture this spectral variation. Because they rely on local spatial averaging, they function as low-pass filters, effectively erasing the high-frequency compressed waves ahead of the source. This results in a smoothed, uniform blob that ignores the directional physics of the moving source.

In contrast, the proposed POCS method (Fig. 3e) successfully reconstructs the Doppler asymmetry. Despite the bandwidth  $\sigma_k$  being tuned globally, the spectral constraint is robust enough to permit the range of wavenumbers generated by the motion. The solver correctly extrapolates the tighter spacing of the leading wavefronts and the wider spacing of the trailing ones, preserving the kinematic signature of the source.

Table 2 provides the quantitative comparison.

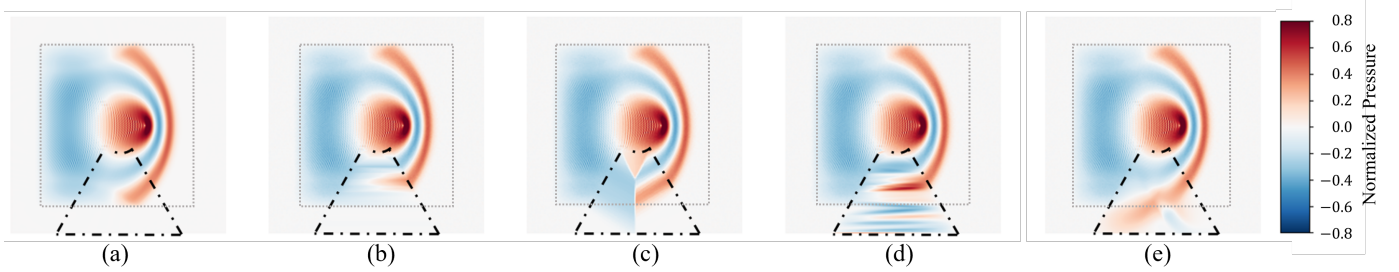


Figure 3: Reconstruction of the Doppler-shifted field ( $M = 0.5$ ) with a wide angular gap. The gray border denotes the sponge layer. (a) Ground Truth showing compressed wavefronts ahead and expanded waves behind. (b) Linear Interpolation. (c) Inverse Distance Weighting. (d) Kriging. (e) Proposed Physics-Constrained POCS. The proposed method (e) successfully reconstructs the spatially varying wavelengths, whereas interpolation methods (b-d) smooth out the high-frequency components.

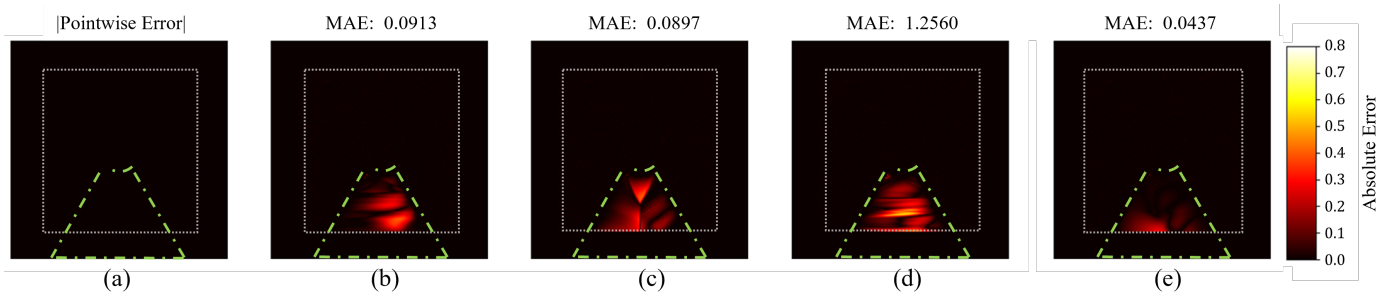


Figure 4: Absolute pointwise error distributions for the Doppler benchmark. The gray border denotes the sponge layer. (a) Reference Scale. (b) Linear Interpolation. (c) IDW. (d) Kriging. (e) Proposed Method. The proposed method significantly reduces error in the high-frequency region ahead of the source.

The proposed method achieves a Mean Absolute Error (MAE) of 0.0437, which is half that of the best baseline (IDW: 0.0897). Globally, the method achieves a Normalized L2 Error of 38.8%, compared to 76.9% for Linear interpolation and over 100% for Kriging. The SSIM score of 80.2% further confirms that the structural details of the frequency-shifted waves are well-preserved. This result demonstrates that the spectral regularization strategy can adapt to spatially varying spectral content induced by source dynamics.

#### 4.3. Rotating Quadrupole Source

The fourth benchmark represents the most complex kinematic scenario: a quadrupole source rotating at 200 Hz with a carrier frequency of 4 kHz. This creates a spiraling interference pattern where the phase relationship is both time-dependent and spatially varying. A wedge-shaped gap is applied to the top sector, obscuring the upward-propagating spiral arms.

Figure 5 illustrates the reconstruction of the swirling pressure field. The ground truth (Fig. 5a) shows distinct, alternating positive and negative spiral arms extending outward from the center.

The geometric baselines (Fig. 5b-d) are unable to replicate this rotational symmetry. Linear interpolation creates sharp, unnatural boundaries. IDW and Kriging effectively low-pass filter the data, resulting in a featureless blur within the gap. They treat the rapid phase alternations of the quadrupole as noise to be smoothed out.

The proposed POCS method (Fig. 5e) is the only approach that successfully reconnects the spiral topology. The solver

propagates the phase information from the valid side lobes into the gap, reconstructing the continuity of the spiral arms.

The quantitative results in Table 3 demonstrate the method's superior performance in capturing dynamic phase structures.

Table 3: Quantitative error metrics for the Rotating Quadrupole benchmark. The proposed method achieves the best performance across all metrics, significantly outperforming geometric interpolation in structural fidelity (SSIM).

Method	MAE	$L_2$ Error (%)	SSIM (%)
Linear	0.1042	42.1%	63.5%
IDW	0.0774	31.5%	62.8%
Kriging	0.1073	49.3%	49.1%
Proposed (POCS)	0.0642	26.0%	78.1%

The proposed method achieves the lowest Normalized  $L_2$  Error of 26.0%, surpassing the best baseline (IDW: 31.5%). This indicates that enforcing the dispersion relation is energetically more accurate than the zero-mean prediction strategy often employed by IDW in oscillatory gaps. Furthermore, the method yields a superior Structural Similarity Index (SSIM) of 78.1%, compared to  $\sim 63\%$  for Linear/IDW. This metric confirms that while geometric methods blur the spiral arms, the proposed solver correctly reconstructs the rotating phase topology.

#### 4.4. Scattering by a Rigid Cylinder

We lastly evaluate the reconstruction capability in a regime dominated by diffraction and interference. The test case involves a rigid cylinder of radius  $r = 0.02$  m immersed in a field generated by a 10 kHz acoustic source located at  $x_s = -0.06$

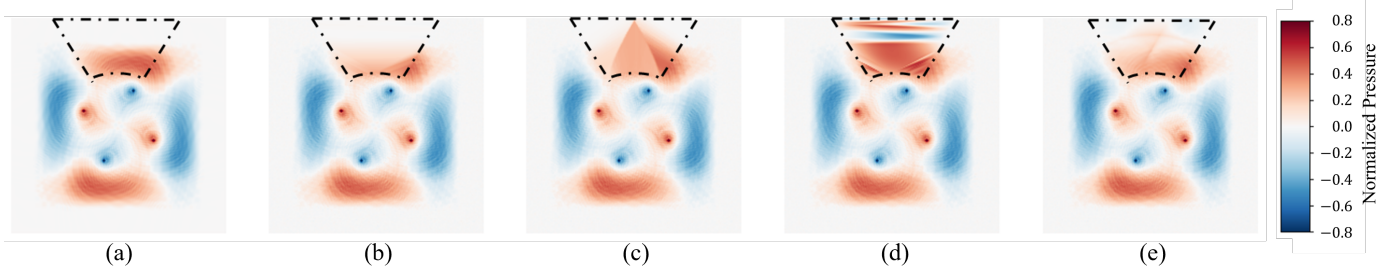


Figure 5: Reconstruction of the rotating quadrupole field (4 kHz tone, 200 Hz rotation). The gray border denotes the sponge layer. (a) Ground Truth showing spiraling wavefronts. (b) Linear Interpolation. (c) Inverse Distance Weighting. (d) Kriging. (e) Proposed Physics-Constrained POCS. The proposed method (e) recovers the coherent spiral arms extending into the gap, while baselines (b-d) produce diffusive artifacts.

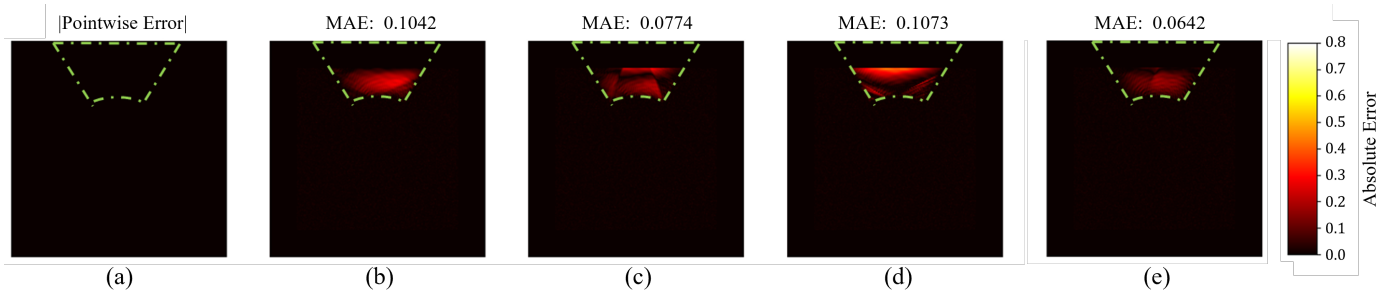


Figure 6: Absolute pointwise error distributions for the rotating quadrupole benchmark. The gray border denotes the sponge layer. (a) Reference Scale. (b) Linear Interpolation. (c) IDW. (d) Kriging. (e) Proposed Method. The proposed method maintains the lowest error in the deep shadow region.

m. This configuration ( $ka \approx 3.7$ ) generates a complex "creeping wave" diffraction pattern into the shadow zone behind the cylinder. The sensor gap is defined as a rectangular region covering the wake, forcing the solver to extrapolate the diffracted wavefronts purely from the illuminated side.

Figure 7 presents the reconstruction results for the 10 kHz snapshot. The ground truth (Fig. 7a) exhibits a characteristic interference pattern in the shadow zone, formed by the superposition of waves diffracting around the top and bottom of the cylinder.

The geometric and smoothness-based baselines fundamentally fail to reconstruct this topology. As seen in Fig. 7(b), Linear interpolation creates a sharp, non-physical cutoff. IDW (Fig. 7c) produces a "cone-like" artifact that diffuses slightly further but lacks phase information. Kriging (Fig. 7d) generates a smooth blur, treating the acoustic field as a diffusive potential rather than a wave.

In contrast, the proposed Physics-Constrained POCS method (Fig. 7e) successfully recovers the oscillatory nature of the field. While the proposed method cannot fully predict the exact scattering dynamics without explicit obstacle modeling, our method captures the dominant acoustic structures within the shadow zone. By enforcing the dispersion relation, the solver prohibits the smooth, non-physical decay observed in the baselines, enabling a plausible physical presumption of the gapped field topology.

The quantitative performance is summarized in Table 4. The proposed method achieves the lowest local error (MAE) and the highest structural similarity (SSIM).

The baseline methods exhibit MAE values ranging from

Table 4: Quantitative error metrics for the Cylinder Scattering benchmark. The proposed method yields the highest SSIM, indicating superior recovery of the diffraction topology.

Method	MAE	$L_2$ Error (%)	SSIM (%)
Linear	0.1577	95.4%	71.2%
IDW	0.1449	92.0%	77.4%
Kriging	0.1587	100.1%	74.5%
Proposed (POCS)	0.1301	84.7%	79.3%

0.1449 to 0.1587, corresponding to the total loss of signal amplitude in the gap. The proposed method reduces the MAE to 0.1301. Crucially, the Normalized  $L_2$  error remains high for all methods ( $> 84\%$ ). This is primarily attributed to amplitude scaling discrepancies inherent to the free-space assumption; the solver tends to underestimate the energy diffracted into the deep shadow of the obstacle. Although our method incurs noticeable quantitative error in magnitude, the SSIM score of 79.3% confirms that it successfully predicts the underlying acoustic field structure and diffraction topology, significantly outperforming the geometric interpolants.

#### 4.5. Sparse Holographic Array Extrapolation

The final benchmark evaluates the capability for “Full-Field Reconstruction” from a sparse circular array. We utilize the same rotating quadrupole source (4 kHz, 200 Hz rotation) but sample the field using only 32 microphones arranged in a ring of radius  $r = 60$  grid units. The goal is to simultaneously interpolate the field inside the ring and extrapolate the radiating wavefronts outside the ring. Since the domain is sampled only

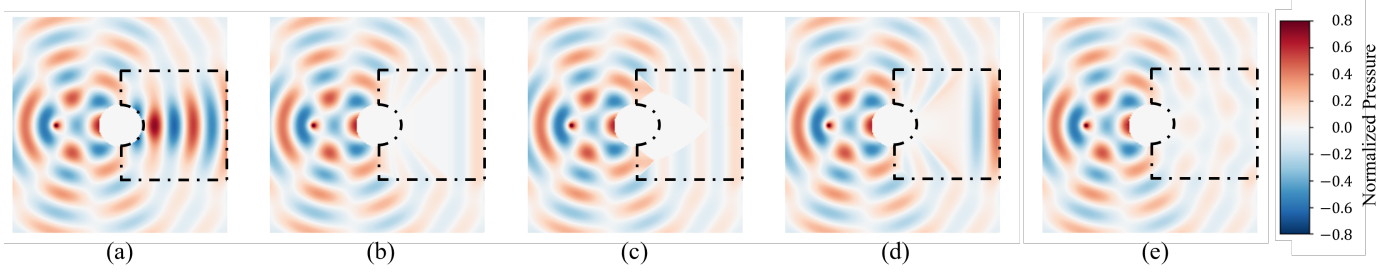


Figure 7: Reconstruction of the 10 kHz scattered field behind a rigid cylinder. The dashed box indicates the sensor-free shadow zone. The gray border region denotes the numerical sponge layer. (a) Ground Truth. (b) Linear Interpolation. (c) IDW. (d) Kriging. (e) Proposed Physics-Constrained POCS. Note that the geometric baselines (b-d) fail to capture the oscillatory interference pattern, producing a diffusive blur, whereas the proposed method (e) recovers the diffractive wave structure.

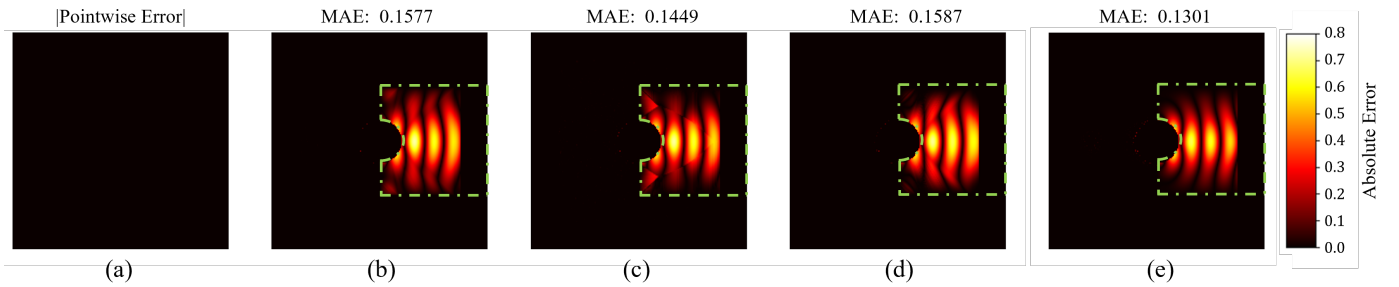


Figure 8: Absolute pointwise error distributions for the cylinder benchmark. The gray border denotes the sponge layer. (a) Reference Pointwise Error Scale. (b) Linear Interpolation. (c) IDW. (d) Kriging. (e) Proposed Method. The proposed method significantly reduces the error magnitude and preserves the wavefront structure compared to the baselines.

at the ring, the reconstruction of the central source region is effectively an inward extrapolation task.

Figure 9 compares the reconstructed fields. The ground truth (Fig. 9a) shows the quadrupole spiral originating from the center and propagating outward past the sensor ring.

The baseline methods exhibit a strong dichotomy between the inner and outer regions. Inside the ring, Linear (b) and Kriging (d) RBFs produce a reasonable approximation of the main lobes, albeit with significant blurring. However, outside the ring, they fail catastrophically. Linear RBFs decay rapidly to the mean, while Kriging (Cubic RBF) explodes numerically due to the unbounded nature of the kernel, creating massive artifacts at the domain boundaries. IDW (c) creates a “starburst” pattern that lacks any wave propagation physics.

In contrast, the proposed POCS method (Fig. 9e) treats the sensors as boundary conditions for the wave equation. It successfully propagates the phase information inward to resolve the source structure and outward to reconstruct the radiating spiral arms. Notably, the proposed method is the only approach that captures the four distinct source poles (visible as alternating red and blue lobes near the center), although with reduced amplitude. While not a perfect reconstruction, this structural recovery contrasts sharply with the baselines, which either blur the center or produce unphysical artifacts.

To rigorously assess the method’s dual capability, we evaluated the Normalized  $L_2$  Error separately for the inner and outer regions.

#### Inner Region (Inward Extrapolation)

The proposed method demonstrates superior performance in the inward reconstruction task, achieving the lowest Inner  $L_2$  Error of 72.0%. This significantly outperforms Kriging (78.8%) and Linear RBF (84.3%), confirming that spectral constraints provide a better regularization for gap-filling than geometric smoothness, even in bounded domains.

#### Outer Region (Outward Extrapolation)

In the outer zone, IDW achieves the lowest numerical error (39.3%). However, this result is deceptive: IDW minimizes error variance by predicting near-zero amplitude away from the sensors (energetically safe), but fails to capture the wave structure. The proposed method achieves a competitive Outer  $L_2$  Error of 46.0% while actively sustaining the wave propagation to the domain boundaries.

The error maps in Figure 10 further illustrate this behavior. The proposed method (e) exhibits a uniform error distribution, whereas baselines like Kriging (d) show severe boundary artifacts. The POCS solver provides the most balanced reconstruction, offering high fidelity in the source region and physically plausible extrapolation in the far field.

## 5. Conclusion

In this work, we addressed the fundamental inverse problem of reconstructing coherent acoustic fields from sparse, irregular,

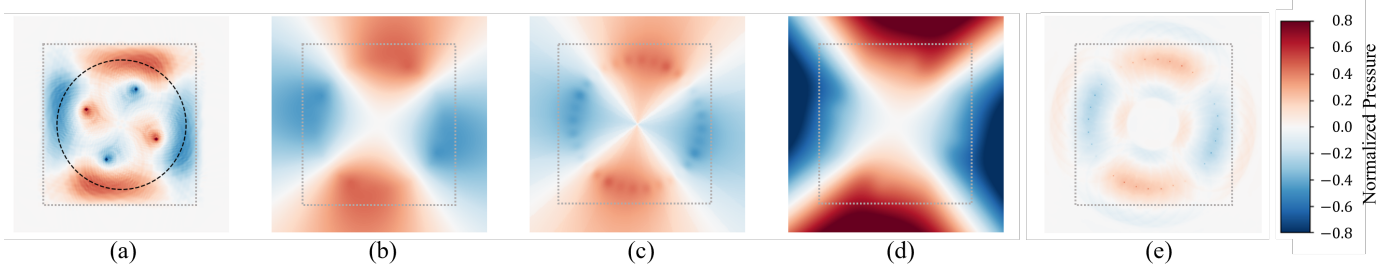


Figure 9: Reconstruction of the full domain from a sparse 32-sensor ring. The gray border denotes the sponge layer. (a) Ground Truth showing the sensor circle. (b) Linear Interpolation (RBF). (c) Inverse Distance Weighting. (d) Kriging (RBF). (e) Proposed Physics-Constrained POCS. The proposed method (e) is the only approach that correctly propagates the wavefronts both inward and outward from the sensor ring.

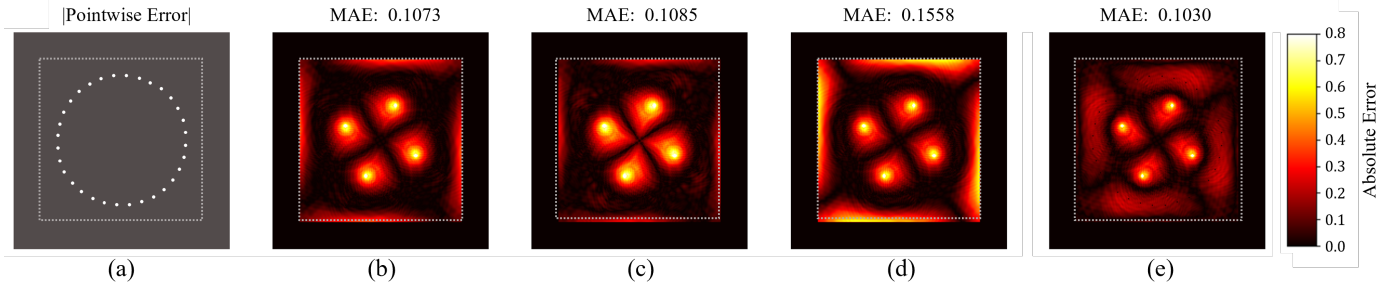


Figure 10: Absolute pointwise error distributions for the sparse array benchmark. The gray border denotes the sponge layer. (a) Reference Scale; white dots indicate microphone positions. (b) Linear. (c) IDW. (d) Kriging. (e) Proposed Method. Note that Kriging (d) exhibits boundary explosions, while the proposed method (e) distributes error evenly across the domain.

and occluded sensor data. Conventional geometric interpolation techniques, such as Kriging and Inverse Distance Weighting, rely on smoothness priors that minimize local curvature. As demonstrated across our benchmarks, these assumptions are inherently ill-suited for oscillatory wave physics. By imposing diffusive decay in unobserved regions, standard interpolants effectively erase the diffraction patterns, interference fringes, and directional lobes that characterize complex aeroacoustic environments.

To overcome these limitations, we proposed a physics-constrained inverse solver based on the method of Projections Onto Convex Sets (POCS). By reformulating the reconstruction as an intersection problem between the set of observation-consistent fields and the manifold of solutions satisfying the acoustic dispersion relation, we derived an iterative algorithm that regenerates missing spectral content without requiring training data or precomputed basis functions.

A systematic evaluation across four canonical scenarios yielded the aggregate performance metrics summarized in Table 6. The proposed method achieves the highest SSIM scores across all test cases, confirming its overall superiority in recovering structural wave topology. Specific insights include:

1. Structural Recovery versus Energy Minimization: While geometric baselines occasionally achieved competitive  $L_2$  error rates by predicting near-zero amplitudes in large gaps—essentially a statistically “safe” guess—they consistently failed to capture topological wave features. In contrast, the proposed method demonstrated superior structural fidelity (Table 6), verifying its ability to reconstruct directional

lobes, spiral arms, and interference nulls that are invisible to regression-based methods.

2. Robustness to Kinematic Complexity: The method proved robust beyond stationary monochromatic sources. In the Doppler (Mach 0.5) and Rotating Quadrupole (200 Hz) benchmarks, the solver successfully reconstructed spatially varying wavenumbers and time-dependent phase topologies. This indicates that the spectral band-pass regularization is sufficiently flexible to accommodate broadband kinematic effects without explicit motion modeling.

3. Bidirectional Extrapolation: The sparse holographic array benchmark highlighted the unique capability of the POCS framework to propagate information bidirectionally. Unlike Radial Basis Functions, which became unstable outside the sensor ring, and IDW, which failed to extrapolate, the proposed method successfully reconstructed the source structure in the center (inward extrapolation) and the radiating wavefronts in the far field (outward extrapolation), maintaining continuity across the sparse aperture.

In positioning this methodology within the broader context of acoustic field reconstruction, it is useful to emphasize its complementary nature. Rather than targeting exact field prediction in highly complex scattering environments, the framework is designed to provide a physically consistent reconstruction in regions where measurements are sparse or unavailable. For example, in the cylinder benchmark—where the rigid obstacle introduces conditions beyond the free-space dispersion model—the method successfully recovers the diffractive structure of the field, even though some amplitude deviations may

Table 5: Statistical Performance for Sparse Array Reconstruction (Full Domain). The  $L_2$  error is split into Inner (Inward Extrapolation) and Outer (Outward Extrapolation) zones to highlight specific solver capabilities. Note: While IDW achieves the lowest Outer error, it does so by predicting near-zero values; the proposed method actively reconstructs the field structure.

Method	Global MAE (Local)	Inner $L_2$ Error (Inward)	Outer $L_2$ Error (Outward)	Global SSIM (Structure)
Linear (RBF)	0.1073	84.3%	56.6%	52.4%
IDW (Sheppard)	0.1085	100.5%	39.3%	53.2%
Kriging (Cubic)	0.1558	78.8%	113.0%	41.9%
Proposed (POCS)	0.1030	72.0%	46.0%	51.3%

Table 6: Comparative Statistical Performance Summary (5 Randomized Trials). The table reports the Mean Normalized  $L_2$  Error (Lower is Better) and Mean SSIM Score (Higher is Better). The proposed Physics-Constrained POCS method consistently outperforms interpolation baselines in structural recovery (SSIM) and total error ( $L_2$ ) for complex wave fields.

Method	Translating Dipole		Doppler Source		Rotating Quadrupole		Cylinder Scattering	
	$L_2$ Error	SSIM	$L_2$ Error	SSIM	$L_2$ Error	SSIM	$L_2$ Error	SSIM
Linear (RBF)	80.0%	57.0%	76.9%	59.4%	42.1%	63.5%	95.4%	71.2%
IDW (Sheppard)	122.3%	64.4%	69.6%	69.1%	31.5%	62.8%	92.0%	77.4%
Kriging (Cubic)	130.8%	44.1%	106.9%	52.3%	49.3%	49.1%	100.1%	74.5%
Proposed (POCS)	<b>14.6%</b>	<b>84.6%</b>	<b>38.8%</b>	<b>80.2%</b>	<b>26.0%</b>	<b>78.1%</b>	<b>84.7%</b>	<b>79.3%</b>

arise due to the simplified physical assumptions.

Accordingly, the proposed POCS solver is best understood as a tool for physically plausible inference, extending valuable structural information into measurement gaps while maintaining strict consistency with both observed data and the governing wave equation. Although it does not aim to restore information entirely lost due to heavy absorption or complex scattering without explicit boundary modeling, it represents a significant step forward compared to geometric interpolation by ensuring that reconstructed regions retain the essential spectral characteristics of acoustic propagation.

Future work will focus on extending this framework to three-dimensional volumetric reconstruction and broadband time-domain formulations, potentially integrating the POCS solver as a differentiable layer within physics-informed neural networks to combine data-driven priors with strict spectral constraints.

## Appendix A: Initialization Strategies and Convergence Acceleration

The Alternating Projection solver is theoretically guaranteed to converge to a solution within the intersection of the constraint sets,  $C_{\text{data}} \cap C_{\text{phys}}$ , provided this intersection is non-empty. However, the convergence rate is governed by the spectral radius of the composite operator  $\mathcal{T}$ . In geometric terms, the POCS algorithm behaves as a pseudo-diffusive process; information propagates from the valid sensor boundary  $\partial\Omega_{\text{valid}}$  into the shadow zone  $\Omega_{\text{gap}}$  at a finite speed determined by the filter bandwidth  $\sigma_k$ .

For large shadow zones, a standard ‘‘Cold Start’’ initialization ( $\mathbf{q}^{(0)} = \mathcal{M}\mathbf{y}$ ) imposes a sharp discontinuity at the gap boundary. This high-wavenumber artifact requires a significant number of

iterations to smooth out. To accelerate convergence, we employ an Interpolation-Based Warm Start.

### A.1 Mathematical Formulation of the Warm Start

Let  $\mathcal{I} : \mathbb{C}^N \rightarrow \mathbb{C}^N$  denote a geometric interpolation operator that maps values from the sparse sensor set  $\Omega_{\text{sensor}}$  to the dense grid  $\Omega$ . The warm start initialization is defined as:

$$\mathbf{q}_{\text{warm}}^{(0)} = \mathcal{I}(\mathcal{M}\mathbf{y}) \quad (23)$$

In contrast to the cold start, where  $\mathbf{q}^{(0)}(\mathbf{x}) = 0$  for  $\mathbf{x} \in \Omega_{\text{gap}}$ , the warm start provides a non-zero support that approximates the low-frequency content of the global field. The POCS solver then acts as a refinement operator, tasked only with recovering the high-frequency diffraction texture rather than the macroscopic amplitude distribution.

### A.2 Inverse Distance Weighting (IDW) Kernel

In our implementation, specifically for scattering benchmarks where shadow zones are geometrically complex, we utilize Inverse Distance Weighting (Sheppard’s Method) as the operator  $\mathcal{I}$ . For any grid point  $\mathbf{x} \in \Omega_{\text{gap}}$ , the field value is estimated as a weighted average of the  $K$ -nearest valid sensors  $\mathcal{N}_K(\mathbf{x}) \subset \Omega_{\text{sensor}}$ :

$$q_{\text{warm}}(\mathbf{x}) = \begin{cases} y(\mathbf{x}) & \text{if } \mathbf{x} \in \Omega_{\text{sensor}} \\ \frac{\sum_{j \in \mathcal{N}_K(\mathbf{x})} w_j(\mathbf{x})y(x_j)}{\sum_{j \in \mathcal{N}_K(\mathbf{x})} w_j(\mathbf{x})} & \text{if } \mathbf{x} \in \Omega_{\text{gap}} \end{cases} \quad (24)$$

The weights  $w_j$  decay according to a Euclidean power law:

$$w_j(\mathbf{x}) = \frac{1}{\|\mathbf{x} - \mathbf{x}_j\|_2^p + \epsilon} \quad (25)$$

where  $p$  is the power parameter (typically  $p = 2.0$  for gravity-model decay) and  $\epsilon$  is a machine-precision constant to prevent singularity. This initialization ensures  $C^0$  continuity across the gap boundary, significantly reducing the initial spectral error  $\|\mathcal{P}_{phys}(\mathbf{q}^{(0)}) - \mathbf{q}^{(0)}\|_2$  before the first iteration of the physics solver.

## Acknowledgement

This research received no external funding

## References

- [1] Olexiy Azarov, Leonid Krupelnitskyi, Hanna Raktyanska, and Jan Fesl. Reconstruction of acoustic surfaces from incomplete data as an identification problem based on fuzzy relations. In *Proceedings of the 2nd International Workshop on Computational & Information Technologies for Risk-Informed Systems (CITRisk 2021)*, volume 3101 of *CEUR Workshop Proceedings*, pages 192–207, Kherson, Ukraine, 2021. CEUR-WS.org.
- [2] Olexiy Azarov, Leonid Krupelnitskyi, and Hanna Raktyanska. Sound field reconstruction from incomplete data by solving fuzzy relational equations. In *Lecture Notes in Computational Intelligence and Decision Making*, volume 1246 of *Advances in Intelligent Systems and Computing*, pages 547–566, Cham, 2021. Springer International Publishing.
- [3] Emmanuel Manu Dabankah, Nicolas Totaro, Claudio Colangeli, and Jérôme Antoni. Acoustic field reconstruction in the presence of masking objects. *Acta Acustica*, 8:40, 2024.
- [4] Pierre Aumond, Arnaud Can, Vivien Mallet, Bert De Coensel, Carlos Ribeiro, Dick Botteldooren, and Catherine Lavandier. Kriging-based spatial interpolation from measurements for sound level mapping in urban areas. *Journal of the Acoustical Society of America*, 143(5):2847–2857, 2018.
- [5] Efren Fernandez-Grande. Four decades of near-field acoustic holography. *Journal of the Acoustical Society of America*, 152(1):R1–R2, 2022.
- [6] J. D. Maynard, E. G. Williams, and Y. Lee. Nearfield acoustic holography: I. theory of generalized holography and the development of NAH. *Journal of the Acoustical Society of America*, 78(4):1395–1413, 1985.
- [7] Earl G. Williams. *Fourier Acoustics: Sound Radiation and Nearfield Acoustical Holography*. Academic Press, London, 1999.
- [8] Sean F. Wu. Methods for reconstructing acoustic quantities based on acoustic pressure measurements. *Journal of the Acoustical Society of America*, 124(5):2680–2697, 2008.
- [9] Donald Shepard. A two-dimensional interpolation function for irregularly-spaced data. In *Proceedings of the 23rd ACM National Conference*, pages 517–524. ACM, 1968.
- [10] Martin D. Buhmann. *Radial Basis Functions: Theory and Implementations*, volume 12 of *Cambridge Monographs on Applied and Computational Mathematics*. Cambridge University Press, Cambridge, 2003.
- [11] Gregory E. Fasshauer. *Meshfree Approximation Methods with MATLAB*, volume 6 of *Interdisciplinary Mathematical Sciences*. World Scientific, Singapore, 2007.
- [12] Pierre Aumond, Arnaud Can, Vivien Mallet, Bert De Coensel, Carlos Ribeiro, Dick Botteldooren, and Catherine Lavandier. Acoustic mapping based on measurements: Space and time interpolation. In *Proceedings of the 46th International Congress and Exposition on Noise Control Engineering (Inter-Noise 2017)*, pages 2287–2298, Hong Kong, China, 2017. Institute of Noise Control Engineering.
- [13] Antoine Lesieur, Vivien Mallet, Pierre Aumond, and Arnaud Can. Data assimilation for urban noise mapping with a meta-model. *Applied Acoustics*, 178:107938, 2021.
- [14] Jørgen Hald. Basic theory and properties of statistically optimized near-field acoustical holography. *Journal of the Acoustical Society of America*, 125(4):2105–2120, 2009.
- [15] Sean F. Wu. On reconstruction of acoustic pressure fields using the Helmholtz equation least squares method. *Journal of the Acoustical Society of America*, 107(5):2511–2522, 2000.
- [16] Sean F. Wu. *The Helmholtz Equation Least Squares Method: For Reconstructing and Predicting Acoustic Radiation*. Modern Acoustics and Signal Processing. Springer, New York, NY, 2015.
- [17] Andreas Schuhmacher, Jørgen Hald, Karsten Bo Rasmussen, and Per Christian Hansen. Sound source reconstruction using inverse boundary element calculations. *Journal of the Acoustical Society of America*, 113(1):114–127, 2003.
- [18] Aaron Towne, Oliver T. Schmidt, and Tim Colonius. Spectral proper orthogonal decomposition and its relationship to dynamic mode decomposition and resolvent analysis. *Journal of Fluid Mechanics*, 847:821–867, 2018.
- [19] Eric C. Hamdan and Filippo Maria Fazi. Focusing phenomena in linear discrete inverse problems in acoustics. *arXiv preprint arXiv:2011.00502*, 2020.
- [20] Marco Olivieri, Mirco Pezzoli, Raffaele Malvermi, Fabio Antonacci, and Augusto Sarti. Near-field acoustic holography analysis with convolutional neural networks. In *Proceedings of the 2020 International Congress on Noise Control Engineering (Inter-Noise 2020)*, volume 261 of *INTER-NOISE and NOISE-CON Congress and Conference Proceedings*, pages 5607–5618, Seoul, South Korea, 2020. Institute of Noise Control Engineering.
- [21] Fei Ma, Sipei Zhao, and Ian S. Burnett. Sound field reconstruction using a compact acoustics-informed neural network. *Journal of the Acoustical Society of America*, 156(3):2009–2021, 2024.
- [22] Marco Olivieri, Mirco Pezzoli, Fabio Antonacci, and Augusto Sarti. A physics-informed neural network approach for nearfield acoustic holography. *Sensors*, 21(23):7834, 2021.
- [23] Efren Fernandez-Grande, Xenofon Karakontantis, Diego Caviedes-Nozal, and Peter Gerstoft. Generative models for sound field reconstruction. *Journal of the Acoustical Society of America*, 153(2):1179–1190, 2023.
- [24] Xenofon Karakontantis, Efren Fernandez-Grande, and Peter Gerstoft. Efficient sound field reconstruction with conditional invertible neural networks. *arXiv preprint arXiv:2404.06928*, 2024.
- [25] Michael J. Bianco, Peter Gerstoft, James Traer, Emma Ozanich, Marie A. Roch, Sharon Gannot, and Charles-Alban Deledalle. Machine learning in acoustics: Theory and applications. *Journal of the Acoustical Society of America*, 146(5):3590–3628, 2019.
- [26] Lev M. Bregman. The relaxation method of finding the common point of convex sets and its application to the solution of problems in convex programming. *USSR Computational Mathematics and Mathematical Physics*, 7(3):200–217, 1967.
- [27] L. G. Gubin, B. T. Polyak, and E. V. Raik. The method of projections for finding the common point of convex sets. *USSR Computational Mathematics and Mathematical Physics*, 7(6):1–24, 1967.
- [28] Athanasios Papoulis. A new algorithm in spectral analysis and band-limited extrapolation. *IEEE Transactions on Circuits and Systems*, 22(9):735–742, 1975.
- [29] Paolo Chiarotti, Milena Martarelli, and Paolo Castellini. Acoustic beam-forming for noise source localization—reviews, methodology and applications. *Mechanical Systems and Signal Processing*, 120:422–448, 2019.
- [30] Noel Cressie. The origins of kriging. *Mathematical Geology*, 22(3):239–252, 1990.
- [31] Martin D Buhmann. Radial basis functions. *Acta Numerica*, 9:1–38, 2000.
- [32] Paul Busch, Teiko Heinonen, and Pekka Lahti. Heisenberg’s uncertainty principle. *Physics Reports*, 452(6):155–176, 2007.
- [33] David Gottlieb and Chi-Wang Shu. On the gibbs phenomenon and its resolution. *SIAM Review*, 39(4):644–668, 1997.
- [34] Roger A Horn. The hadamard product. In *Proceedings of Symposia in Applied Mathematics*, volume 40, pages 87–169, 1990.
- [35] David F Watson. Computing the n-dimensional delaunay tessellation with application to voronoi polytopes. *The Computer Journal*, 24(2):167–172, 1981.
- [36] Donald Shepard. A two-dimensional interpolation function for irregularly-spaced data. In *Proceedings of the 1968 23rd ACM National Conference*, pages 517–524. ACM, 1968.
- [37] Alain Hore and Djemel Ziou. Image quality metrics: Psnr vs. ssim. In

2010 20th International Conference on Pattern Recognition, pages 2366–2369. IEEE, 2010.